

Non-Volatile Reconfigurable Integrated Photonics Enabled by Broadband Low-Loss Phase Change Material

Zhuoran Fang,* Jiajiu Zheng, Abhi Saxena, James Whitehead, Yueyang Chen, and Arka Majumdar*

Phase change materials (PCMs) have long been used as a storage medium in rewritable compact disk and later in random access memory. In recent years, integration of PCMs with nanophotonic structures has introduced a new paradigm for non-volatile reconfigurable optics. However, the high loss of the archetypal PCM $\text{Ge}_2\text{Sb}_2\text{Te}_5$ in both visible and telecommunication wavelengths has fundamentally limited its applications. Sb_2S_3 has recently emerged as a wide-bandgap PCM with transparency windows ranging from 610 nm to near-IR. In this paper, the strong optical phase modulation and low optical loss of Sb_2S_3 are experimentally demonstrated for the first time in integrated photonic platforms at both 750 and 1550 nm. As opposed to silicon, the thermo-optic coefficient of Sb_2S_3 is shown to be negative, making the Sb_2S_3 -Si hybrid platform less sensitive to thermal fluctuation. Finally, a Sb_2S_3 integrated non-volatile microring switch is demonstrated which can be tuned electrically between a high and low transmission state with a contrast over 30 dB. This work experimentally verifies prominent phase modification and low loss of Sb_2S_3 in wavelength ranges relevant for both solid-state quantum emitter and telecommunication, enabling potential applications such as optical field programmable gate array, post-fabrication trimming, and large-scale integrated quantum photonic network.

1. Introduction

Traditional means of tuning silicon photonic integrated circuits (PICs) primarily rely on thermo-optic or free carrier dispersion effect. Thermo-optic phase shifters built on silicon-on-insulator (SOI) platform have achieved device footprint $<10 \mu\text{m}^2$ but are slow and power hungry (See Table 1). Phase shifters based on free carrier dispersion effect can significantly reduce the power consumption and increase the modulation speed but suffer in

terms of large device length ($>100 \mu\text{m}$) as a result of small refractive index change (usually $\Delta n < 10^{-3}$).^[2,3] To overcome these limitations, the silicon photonics community has started to head toward a hybrid approach where foreign materials are integrated with SOI waveguides to act as a tuning medium.^[4] One of the promising candidates is organic electro-optic (EO) polymer which exhibits large Pockels effect and fast tuning speed.^[5-7] However, these organic compounds have tendency to degrade at temperature $>100 \text{ }^\circ\text{C}$, which renders them unsuitable to interface with the active electronics that heat up during the operation. Lithium Niobate (LN), an EO material which has long been used in free-space EO modulators, has recently gained traction thanks to the development of advanced dry etching techniques, which lead to extreme low-loss (0.25 dB cm^{-1}) waveguides.^[8] The complementary-metal-oxide-semiconductor (CMOS) compatibility of LN also makes it attractive for large-scale PIC.^[9] Nevertheless, devices based on LN tend to have large footprint

($>1 \text{ mm}$) due the minimal refractive index change as a result of small Pockels coefficient. Nano-opto-electro-mechanical (NEOM) devices^[10] based on plasmonic-silicon hybrid waveguide offer attojoule switching and small footprint but are relatively slow in operation. Additionally, mechanical devices often suffer from low yield and reliability issues. Silicon-plasmonic modulators that harness the free-carrier dispersion effect of ITO^[11] can support operation speed up to 1.1GHz and have device footprint down to $1.4 \mu\text{m}$ but often suffer from high insertion loss. Finally, all the aforementioned tuning methods are volatile, necessitating a constant supply of the electric power. Although memristor switch based on the filamentation of amorphous silicon^[12] can provide non-volatility, it is plagued by high insertion loss and has very slow switching speed.

Phase change materials (PCMs) can mitigate these fundamental limitations, thanks to the non-volatile phase transition and strong index modulation (typically $\Delta n > 1$), and thus can enable reconfigurable PICs for various applications including photonic switches,^[13,14] photonic memory,^[15] optical computing,^[16] and optical neural network.^[17] The suitability of PCMs for application in non-volatile reconfigurable photonics comes from its large contrast in complex refractive index upon

Z. Fang, Dr. J. Zheng, A. Saxena, J. Whitehead, Y. Chen, Prof. A. Majumdar
Department of Electrical and Computer Engineering
University of Washington
Seattle, WA 98195, USA
E-mail: rogefzr@uw.edu; arka@uw.edu

Prof. A. Majumdar
Department of Physics
University of Washington
Seattle, WA 98195, USA

 The ORCID identification number(s) for the author(s) of this article can be found under <https://doi.org/10.1002/adom.202002049>.

DOI: 10.1002/adom.202002049

Table 1. Comparison of different tuning mechanisms used in integrated silicon photonics. The areas that GST is superior to are highlighted in red.

Tuning medium	Tuning method	Operation mode	Energy per bit	Speed	Insertion loss [dB]	Length of active region	Scalability	High temperature operation	Nonvolatility
Si ^[1]	Thermo-optic	Monolithic	30.5 nj	≈100 kHz	0.5	10 μm	✓	✓	×
Si ^[3]	Free-carrier dispersion, PN	Monolithic	4.2 pj	≈20 GHz	7.4	1 mm	✓	✓	×
Si ^[2]	Free-carrier dispersion, PIN	Monolithic	5 pj	≈9 GHz	12	0.1 mm	✓	✓	×
Au ^[10]	NOEM	Plasmonic and cavity-assisted	130 aj	≈12 MHz	0.1	10 μm	✓	✓	×
EO polymer ^[5,7]	Electro-optics	Hybrid	0.7 fj	>100 GHz	2	0.5 mm	×	×	×
Lithium Niobate ^[9]	Electro-optics	Hybrid	170 fj	>70 GHz	2.5	3 mm	✓	✓	×
ITO ^[11]	Free-carrier dispersion	Plasmonic	2046 fj	1.1 GHz	6.7	1.4 μm	✓	✓	×
Si ^[12]	Filamentation	Plasmonic	750 μj	≈kHz	4.2	5 μm	✓	✓	✓
GST ^[13,14]	Material phase change	Cavity-assisted	11 nj, 86 nj ^{-1 a)}	≈10 MHz	1.8 ^{b)}	<5 μm	✓	✓	✓

^{a)}11 nj for amorphization and 86 nj for crystallization. ^{b)}Quoted for 5 μm long, 20 nm thick GST on a microring.

phase transition,^[18] long-term stability of multiple crystallographic phases,^[19] reversible switching between the amorphous and crystalline states by both optical and electrical means,^[19] cyclability of up to 10¹⁵,^[20] sub-nanosecond switching speed,^[21] and low switching energy.^[22]

Among various PCMs, Ge₂Sb₂Te₅ (GST) is by far the most studied material in integrated photonics.^[23] Table 1 compares the performance metrics of a GST-based integrated photonic switch^[13,14] with other popular tuning mechanisms for silicon photonics. While GST provides clear advantages over other tuning mechanisms in terms of power consumption and compact size, the performance of GST–SOI based integrated photonics is fundamentally limited by strong band to band absorption in the visible wavelengths and the near-IR (see Table 2 and Insertion loss in Table 1). Therefore, GST becomes impractical for large-scale PIC platforms^[24,25] and optical Field Programmable Gate Arrays (FPGAs)^[26,27] where light is guided through numerous phase change photonic routers. While device engineering can circumvent some of the losses at 1550 nm,^[28,29] this comes at the expense of increased device length, and such approach does not work near visible wavelength, where the optical loss is very large. A PCM with wide bandgap can overcome these limitations. In this paper, we investigate a wide bandgap PCM Sb₂S₃ which exhibits broadband transparency from 610 nm to near-IR.^[30] The strong optical phase modulation and low optical loss of Sb₂S₃ are experimentally demonstrated for the first time on two different integrated photonic platforms: Silicon Nitride (SiN) and SOI at 750 and 1550 nm, respectively. As opposed to silicon, the thermo-optic

coefficient of Sb₂S₃ is shown to be strongly negative, making the Sb₂S₃–SOI hybrid platform less sensitive to thermal fluctuation. Finally, a Sb₂S₃ integrated non-volatile microring switch is demonstrated which can be tuned electrically between a high and low transmission state with an extinction ratio of over 30dB. The work experimentally verified the prominent optical phase modification and low loss of Sb₂S₃ (abbreviated as SbS in the rest of the paper) in a broad wavelength range, enabling potential applications such as optical FPGAs,^[26,27] post-fabrication trimming,^[31] and large-scale integrated quantum photonic networks.^[32]

2. Results and Discussion

2.1. Materials Characterization

Four samples of 100 nm-thick SbS were deposited by sputtering (see Experimental Section) on silicon substrates and were later annealed for 20 mins at four different temperatures, ranging from 423 to 573 K. The optical constants of SbS in amorphous and crystalline states were first measured by ellipsometry (Figure 1a) for optical mode simulation. The phase transition is confirmed in both X-ray diffraction (XRD) (Figure 1b) and Raman spectroscopy (Figure 1c). We found that the material started to crystallize at ≈523 K and continued to crystallize through 573 K, as seen from the emerging XRD peaks in Figure 1b. The Bragg diffraction angles 2θ that give rise to constructive interference match with previous literature^[35–38]

Table 2. Comparison of Δn and k_c of Sb₂S₃, Sb₂Se₃, GST, and GSST at 633 and 1550 nm. k_c (extinction coefficient) is quoted for the crystalline state of the PCM. Δn is the refractive index change from amorphous to crystalline state.

	Δn at 633 nm	k _c at 633 nm	Δn/k _c at 633 nm	Δn at 1550 nm	k _c at 1550 nm	Δn/k _c at 1550 nm
GST ^[13]	0.16	3.82	0.04	2.74	1.09	2.51
GSST ^[33]	0.62	2.56	0.24	1.75	0.42	4.17
Sb ₂ Se ₃ ^[34]	1.12	1.40	0.8	0.76	0	Undefined
Sb ₂ S ₃	0.87	0.56	1.55	0.54	0.05	10.8

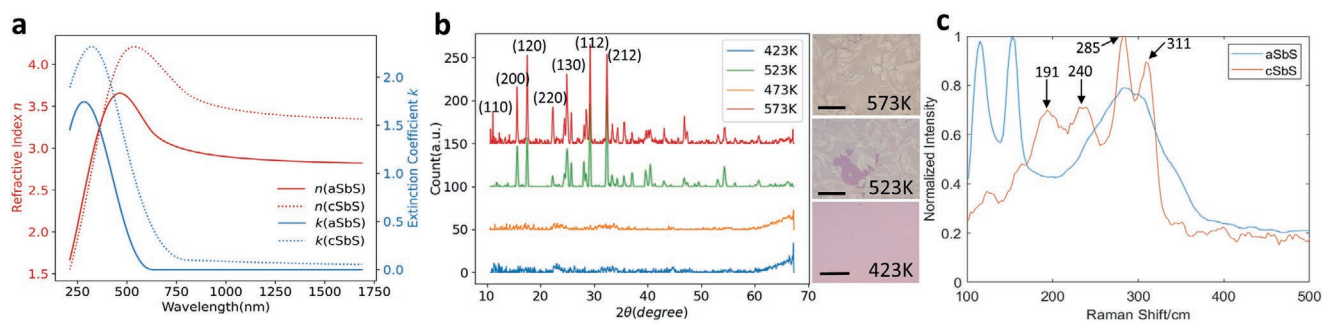


Figure 1. Material characterization of SbS. a) Fit refractive index (n) and extinction coefficient (k) of 100 nm SbS in amorphous and crystalline states. b) X-ray diffraction spectrum of SbS annealed at four different temperatures for 20 min. Characteristic diffraction peaks are indexed based on literatures. The right panel shows the morphological evolution of SbS polycrystal grains as the annealing temperature increases (scale bar is 200 μm). c) Raman spectrum of amorphous and crystalline (annealed at 573 K) SbS. The characteristic Raman shifts of cSbS are indexed according to the literature.

and correspond to the characteristic crystallographic planes in typical SbS crystals. The optical micrographs (right panel of Figure 1b) support the XRD results, showing the nucleation and growth of SbS polycrystalline domains with increasing temperature. The grain growth was incomplete at 523 K and reached a completion at 573 K. This is further corroborated by the Raman spectrum showing the characteristic Raman shift in both as-deposited amorphous and annealed crystalline SbS, denoted as aSbS and cSbS, respectively, with good match to the previous literatures.^[36,38]

The minimal optical loss of SbS originates from its wide bandgap^[30] ($\approx 1.7\text{--}2\text{eV}$), which leads to suppressed band to band absorption from 610 nm. Even in its crystalline state, SbS exhibits low loss ($k \approx 0.05$) at 1550 nm. This is superior to the recently-reported broadband transparent GSST^[33,39,40] which has near-zero loss at 1550 nm in amorphous state but suffers from non-negligible loss in the crystalline state (see Table 2). Another emerging PCM Sb_2Se_3 has near zero loss in both states near 1550 nm^[34] but is plagued by the bandgap absorption in the visible range and hence exhibits measurable losses near 633 nm. One potential limitation for SbS, however, is the simultaneous reduction in both Δn and k , as a result of Kramers–Kronig relation, and hence smaller phase shift per unit length. However, this could be easily overcome by using longer or thicker SbS (as discussed later in the paper), thanks to the reduced optical absorption.

The effective index and mode profiles of the waveguides with different thicknesses of SbS on SOI waveguide are simulated using Lumerical Mode Solutions to find the optimal thickness. Here, the ellipsometry data from 20 nm SbS is used instead (see Section S1, Supporting information). Figure 2a,b shows that the fundamental quasi-transverse electric (TE) mode at 1550 nm is confined in the waveguide and there is a large effective index change ($\Delta n_{\text{eff}} \approx 0.022$) due to the phase transition of 20 nm SbS. Thanks to the low loss of SbS, we get a large ratio between the effective index change and the loss at the crystalline state ($\frac{\Delta n_{\text{eff}}}{k_{\text{eff}}} \approx 4.183$). Note that the final capping layer of

10 nm SiN is not considered in the reported simulation. The extra SiN capping raises the effective index by 0.06 but does not change the Δn_{eff} and loss. The increased imaginary part in cSbS indicates the increase of optical absorption in the crystalline state. We also plot the change of effective index and

optical absorption as a function of SbS thickness (Figure 2e). The index contrast increases with increasing PCM thickness (as the optical mode has stronger interaction with the PCM) but the optical absorption also becomes larger. This is illustrated in Figure 2c,d with 66 nm of SbS integrated on silicon waveguide ($\Delta n_{\text{eff}} \approx 0.038$ and $\frac{\Delta n_{\text{eff}}}{k_{\text{eff}}} \approx 3.98$). Based on our simulation, we chose the SbS thickness as 20 nm to reduce the excess loss ($\alpha = \frac{4\pi k_{\text{eff}}}{\lambda} = 0.185 \text{ dB } \mu\text{m}^{-1}$ and $\Delta n_{\text{eff}} \approx 0.022$). The index contrast far surpasses the typical Si thermal phase shifter which can only achieve $\Delta n_{\text{eff}} < 1.8 \times 10^{-4}$ per Kelvin change in temperature.^[41] The 20nm thickness is also chosen to facilitate the thermal diffusion as the PCM needs to be quenched rapidly during amorphization so thinner film has faster cooling rate.^[42]

2.2. SbS on Si Microring Resonators

Varying lengths of 20 nm and 66 nm thick SbS are deposited on Si microring resonators of radius 20 μm (device schematic shown in Figure 2f) using standard fabrication techniques (See Experimental Section). The insets show the optical micrograph of Si microring patterned with 10 μm -long, 20 nm-thick SbS and the cross-section of the device. The PCM is capped with 10 nm of PECVD SiN to prevent oxidation during annealing.

The phase shift induced by GST^[13] and different thicknesses of SbS near 1550nm are compared in Figure 3a where the length of PCM is fixed at 10 μm . It can be seen that due to the high loss of cGST ($\alpha = 7.6 \text{ dB } \mu\text{m}^{-1}$), the resonance is completely destroyed at crystalline state, whereas the resonance is clearly visible for the 20 nm and 66 nm thick cSbS capped rings, implying that cSbS has much lower optical loss than GST. This demonstrates that SbS could potentially be used to build optical phase shifter^[43] that operates based on electrorefractive modulation. The spectral shift caused by phase transition of 66 nm SbS is 0.93 nm compared to 0.53 nm for 20nm SbS, giving rise to 75% increase in the shift. This is very close to the 73% increase in Δn_{eff} predicted by the mode simulation (Figure 2a–d). It is also worth pointing out that the microring is designed to be critically coupled at crystalline state which is the reason why the extinction ratio of the resonance increases dramatically as a result of the enhanced loss due to the phase transition. Figure 3b shows how the spectral shift and extinction

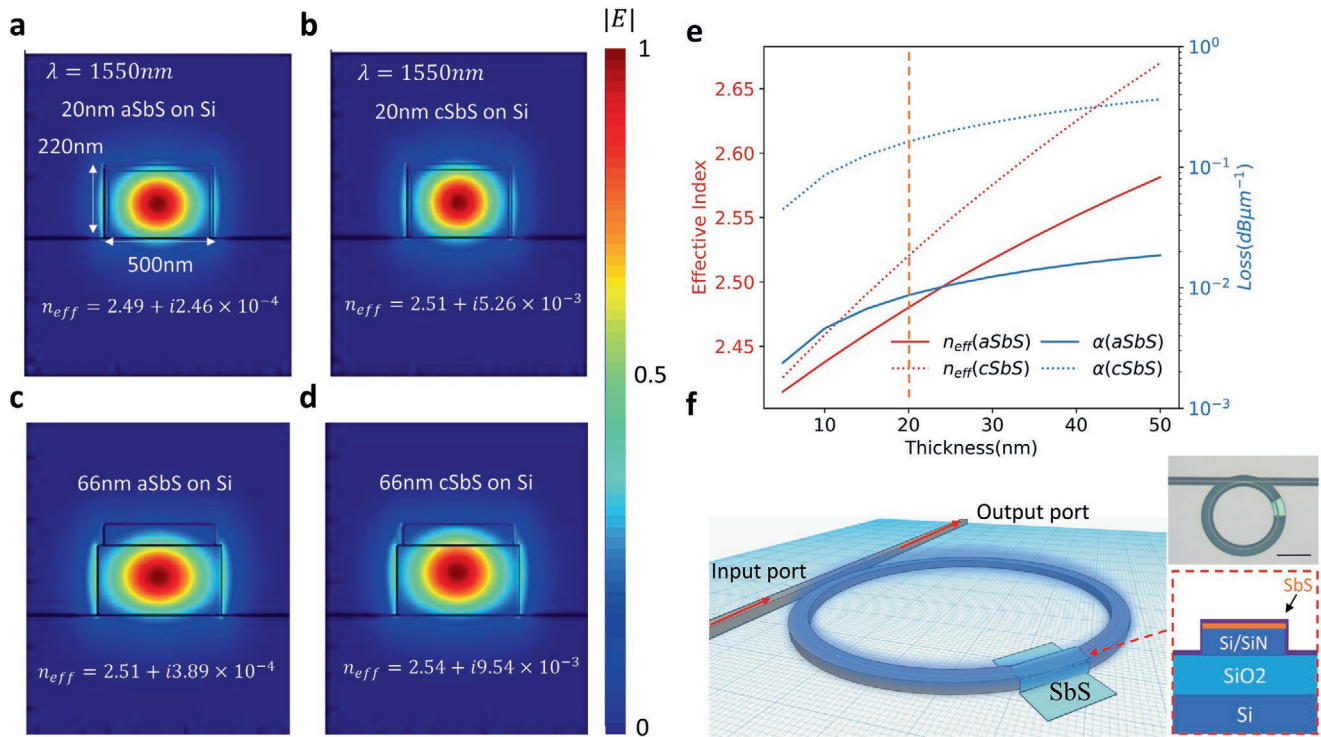


Figure 2. Optical mode simulation of SbS on SOI. a,b) Simulated fundamental TE mode profiles of 20 nm aSbS/cSbS on SOI hybrid waveguide at 1550 nm using the optical constants extracted from ellipsometry. Note here that the waveguide sidewalls are also covered with SbS (to be consistent with the experiments reported later in the paper). c,d) Simulated fundamental quasi-TE mode profiles of 66 nm aSbS/cSbS on SOI hybrid waveguide at 1550 nm. Here, SbS is only placed on top of the waveguide to be consistent with the experiment. e) Variation of effective index and absorption coefficient with the SbS thickness. f) Schematic of microring resonators with SbS patterned on the ring. The inset shows optical micrograph (scale bar: 20 μm) of SbS-capped ring and the cross-section of the device.

ratio evolved as the length of 66 nm-thick SbS increases from 0 to 50 μm across the telecommunication C-band. The red shift becomes increasingly large such that the resonance eventually shifts over one free spectral range of the microring at 50 μm . The rise in optical loss with length is confirmed by the transition from overcoupling (small resonance dip) at 0 μm , near critical coupling (maximum dip) at 10 μm , and strong undercoupling (small dip) at 50 μm . Notice that a red shift (≈ 0.83 nm) is seen on the 0 μm one (i.e., no SbS) due to a global capping of PECVD SiN before thermal annealing, which does not affect our conclusion as the capping layer is lossless and affects all the devices equally.

To analyze the optical phase modulation effect and loss quantitatively, the resonance dip near 1550 nm is fit with a Lorentzian function to extract the quality factor (Q) and the loss (Figure 3c). The optical phase modulation effect is quantified as the spectral shift $\Delta\lambda$ from aSbS to cSbS, while the attenuation is extracted from the Q factor reduction from amorphous to crystalline state. The results are plotted in Figure 3d,e. The experimental data shows a good linear fit where the red shift due to the SbS phase transition increases linearly with the length of SbS. The spectral shift per unit length of SbS is extracted to be 0.060 ± 0.006 nm μm^{-1} . The loss introduced by SbS is estimated from the Q factors using the relation:^[13]

$$\text{Loss} = 2\pi R \frac{2\pi n_g}{\lambda_0} \left(\frac{1}{Q} - \frac{1}{Q_0} \right) = \frac{2\pi\lambda_0}{\text{FSR}} \left(\frac{1}{Q} - \frac{1}{Q_0} \right) \quad (1)$$

where n_g is the group index, Q is the quality factor of the ring after SbS phase transition, and Q_0 is the Q factor of the ring with as-deposited SbS; FSR is the free spectral range. The loss of cSbS (orange line) increases linearly with the PCM length whereas the aSbS (blue line) remains almost flat, signifying extremely low loss as also confirmed by the mode simulation (Figure 2a). The attenuation of cSbS is estimated to be 0.16 ± 0.02 dB μm^{-1} , almost 50 times smaller than that of cGST.^[13]

The spectral shift induced by PCM on ring can be numerically calculated using the following equation:^[13]

$$\frac{\Delta\lambda}{L_{\text{SbS}}} = \frac{\Delta n_{\text{eff}} \lambda_0}{2\pi R n_{\text{eff}0}} \quad (2)$$

where R is the radius of the microring, λ_0 and $n_{\text{eff}0}$ are the resonance wavelength and effective index before phase change, respectively. Δn_{eff} due to SbS phase change is extracted from the mode simulation as discussed above. The simulation results are compared with the experimental results in Table 3.

The extracted Δn_{eff} from the experiment is 0.012 compared to 0.022 from simulation (which uses the ellipsometry data from blanket SbS measurement). This reflects a potential deviation of material optical properties, especially the real part of refractive index, as the PCM shrinks down from 1 by 1 cm blanket film (used for ellipsometry) to thin nanoscale patches on waveguides. Similar deviation has also been previously reported in

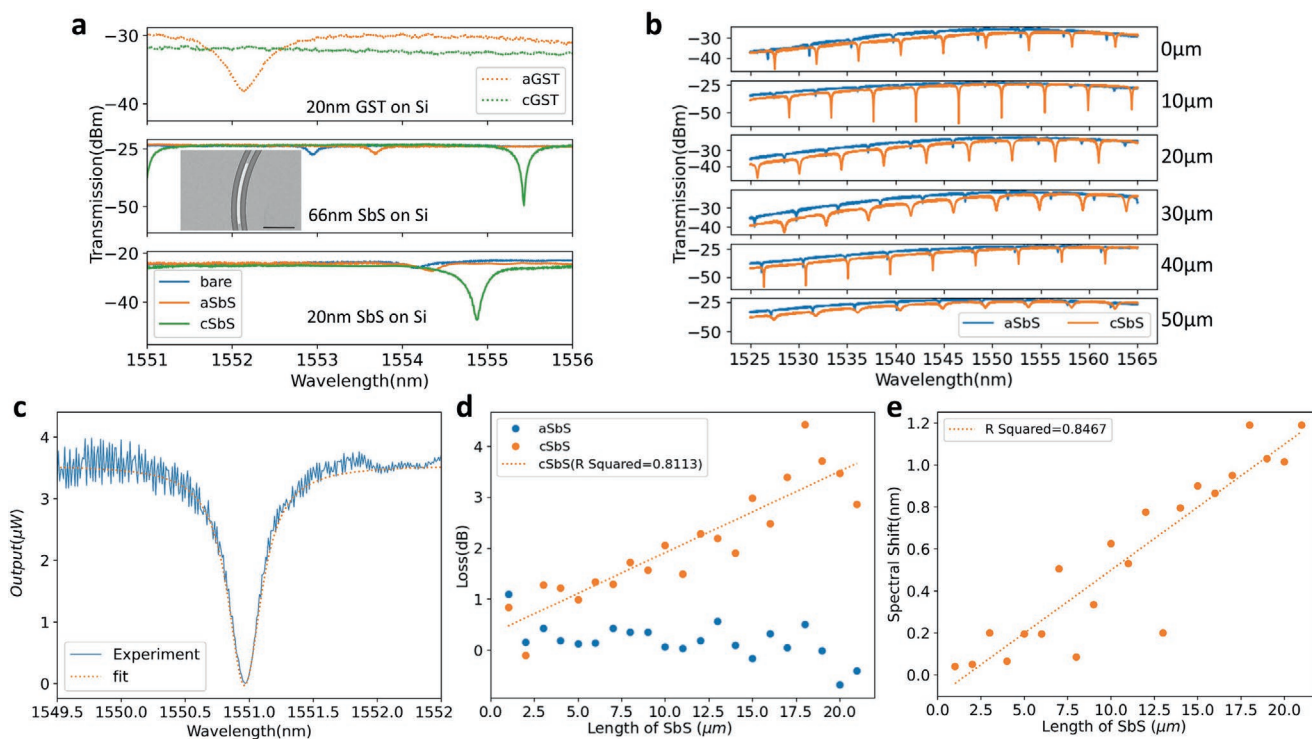


Figure 3. SbS on Si microring resonators. a) Optical spectrum of microring resonators capped with 20 nm GST (top), 66 nm SbS (middle), and 20 nm SbS (bottom) in amorphous and crystalline states. The length of the microring resonator is 10 μm . The inset of middle plot shows the SEM of 66 nm SbS placed only on top of the waveguide (scale bar: 5 μm). b) Transmission of ring resonators over the C band for increasing length of 66 nm aSbS and cSbS on SOI. 0 μm indicates the absence of SbS (i.e., a bare ring). c) Lorentzian fitting of measured resonance dip of Q factor \approx 5000. d) Optical loss of 20 nm thick aSbS and cSbS on SOI at various lengths. e) Spectral shift from amorphous to crystalline with increasing length of 20 nm thick SbS on SOI.

nano-patterned GST.^[13] Another possible explanation is the change of SbS composition upon thermal annealing due to the Sulfur loss.^[35] Although we have verified that the stoichiometry change is small for 100 nm SbS upon thermal annealing (See Section S2, Supporting information), it is hard to rule out the effect of composition change in 20 nm SbS. It is possible that only the surface PCM suffers from composition variation, so the measured composition change is small for 100 nm SbS. For 20 nm SbS, such variation, if indeed exists, may lead to more prominent deterioration of device performance. Finally, the non-uniform coverage of SbS on the waveguide sidewall could also be a contributing factor – SbS deposited on the sidewall is likely to be thinner than on the top of the waveguide due to the slight directional nature of the sputtering (See Section S3, Supporting information). On the other hand, the ellipsometry does predict the imaginary part of refractive index accurately which implies that the material's optical loss does not vary significantly as the dimensions reduce. The extracted loss is higher than what was found in the previous work^[34] where SbS was also capped on Si waveguides. This higher loss can be attributed to surface oxidation or Sulfur

migration due to the thin (10 nm) capping layer used. Thicker encapsulation (>50nm) could prevent this in future. The result shown here provide an insight to the design of PCM based photonic devices where the discrepancy between nano-patterned and the bulk material's optical properties must be considered.

2.3. Electrical Switching of SbS

To demonstrate the feasibility of an active integrated device based on SbS, an ITO external heater is patterned on top of the PCM to achieve on-chip electrical actuation of SbS phase transition (see Experimental Section for fabrication details and the optical characterization setup), as shown in **Figure 4a**. On-chip electrically switching has advantages over excitation by free-space laser^[34] or waveguide optical switching,^[44] because it does not require the complex alignment process of free-space setup while it allows scale-up of the PICs with increased compute density. Additionally, as low-loss PCMs like SbS do not absorb light near 1550 nm, green or even blue laser must be used for optical switching, in which case the light will not be guided within the waveguides designed for near IR. While other means of electrical switching mechanisms^[14,45,46] have been harnessed for tuning PCMs in integrated photonics, ITO microheater^[47–49] has the benefits of high electrical conductivity, low optical loss from visible to near IR, and easy integration via sputtering. By applying voltage pulses across the ITO, electrical current causes Joule heating and subsequently phase transition

Table 3. Comparison between the simulation and experimental results.

	Simulation	Experiment
$\Delta\lambda$ [nm/ μm]	0.109	0.060 ± 0.006
$\Delta\alpha$ [dB/ μm]	0.185	0.160 ± 0.018

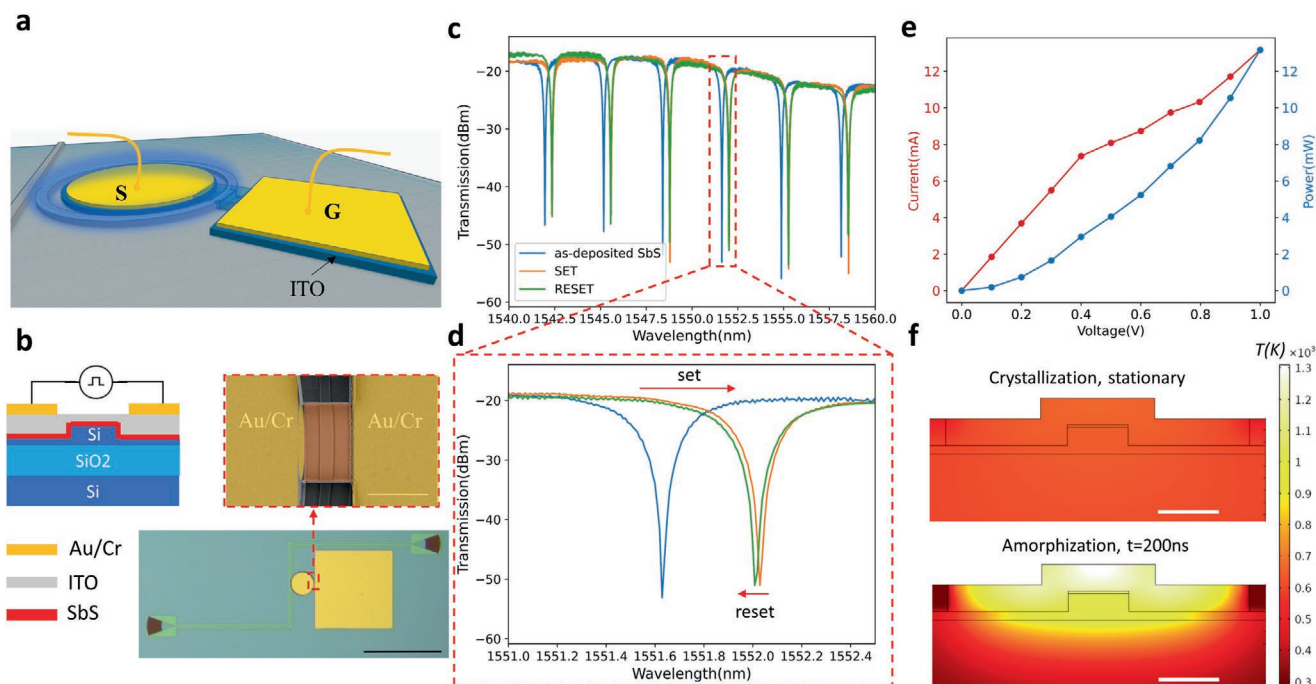


Figure 4. Electrical switching of SbS. a) Schematic of integrated photonic microring switch based on SbS. b) Cross-section of the device, optical micrograph (scale bar: 200 μm) and false color SEM (scale bar: 3 μm) of the fabricated device. c,d) Transmission spectrum showing the SET and RESET operation as red and blue shift of the resonance dip. e) I – V curve (red) and power (blue) during a 0–1 V DC sweep that triggered the SET operation. f) Temperature distribution under stationary heating at 1 V (top) and after 200 ns pulse at 6 V (bottom). Scale bar is 500 nm.

of the PCM. Here, a microring modulator design^[50] is adopted to amplify the modulation effect of SbS. The Si waveguide is partially etched by 140 nm, as opposed to fully etched, to leave an 80 nm-thick Si slab which acts as a heat sink to facilitate thermal diffusion from the PCM. It also helps the lift-off of ITO film as thinner ITO can be used to ensure conformal step coverage. The false color SEM in Figure 4b shows a fabricated device where the Si waveguide is conformally covered with ITO. The SbS is deposited beneath the ITO, and hence is not visible in the SEM. Figure 4c,d demonstrates the electrical switching of 8 μm -long SbS into its crystalline state by a DC voltage sweep from 0 to 1 V at power of 13 mW. The I – V curve in Figure 4e shows a relatively linear relationship – a proof that ITO has stable resistance over this voltage/temperature range. Heat transfer simulation^[42] in Figure 4f (top) shows the temperature distribution under stationary heating from a DC voltage of 1 V. The temperature reaches 650 K which is higher than the crystallization temperature but lower than the melting point of SbS. The DC sweep allows extended period for long range atomic diffusion, during which the atoms can settle in the most energetically favorable positions. The red shift is a result of PCM phase transition because it was found that the refractive index of amorphous ITO remains relatively constant upon heating up to 773 K^[51] while the thermo-optic effect is volatile. The spectral shift of 0.4 nm matches very well with the predicted shift of 0.39 nm based on simulation of rib waveguide (see Section S4, Supporting information) but lower than what was measured from fully etched waveguide (0.48 nm) due to less mode confinement. However, since the ring is designed to be critically coupled at crystalline state, it is still large enough to give an extinction ratio of over 30 dB in optical transmission with

minimal increase in the resonance linewidth. The strong phase modulation at a cost of small loss shows that SbS is a promising tuning medium for next-generation non-volatile large-scale PICs.

The device can be reset by applying a 6 V 200 ns square pulse using a function generator, causing a slight blue shift. The bottom plot of Figure 4f shows the simulated temperature distribution after a 200 ns 6 V square pulse is applied. The temperature at the top layer of SbS has reached over 1000 K, more than what is required for amorphization and below the melting point of Si waveguide, which is confirmed by plotting PCM temperature against time (Figure S4c, Supporting information). The trailing edge of the pulse was set to be 8 ns to allow the melt-quench of the PCM during which the fast-moving atoms are quickly frozen into a disordered state. However, the RESET spectrum does not perfectly overlap with the original spectrum while the Q factor remains roughly the same as the SET spectrum. We speculate that the abrupt resistivity increase of ITO at 650 K^[52] gives rise to regional thermal hot spots that cause nonuniform heating of the PCM. Pulses of higher voltages led to further blue shift and broadening of resonance dip, which implies that the PCM amorphization is accompanied by waveguide damage, as some local hotspots may have temperature exceeding the melting point of Si (See Figure S5, Supporting information). Since the cyclability of blanket film SbS has been recently reported using laser pulses,^[34,53] we believe the low cyclability of our device is more of a heater design issue rather than SbS's material issue. Transparent conductors whose conductivity is thermally stable such as graphene^[54] and FTO^[55] could provide a better solution for operation with large number of cycles.

Table 4. Comparison between SbS, GST, and GSST integrated microring switch.

	Insertion loss [dB]	Length of active region [μm]	PCM thickness [nm]
SbS (this paper)	0.48	8	20
GST ^[13]	1.80	5	20
GSST ^[33]	<0.5	10	50

The switching time for the SET operation is 1s, which is the duration of 0–1 V voltage sweep, while the switching time for RESET is 200 ns, which is the pulse width. Such relatively slow switching speed is however not limited by the fundamental PCM properties but by the thermally unstable heater material and unoptimized heater design (i.e., thermal diffusion is impeded by the thick ITO). In the future, the waveguides can be planarized to reduce the required heater material thickness or atomically thin heater such as graphene can be used. The room-temperature thermal conductivity^[56] of cSbS is $1.2 \text{ W m}^{-1} \text{ K}^{-1}$ (vs $0.6 \text{ W m}^{-1} \text{ K}^{-1}$ of cGST), while the heat capacity at constant pressure^[57] of cSbS is $353 \text{ J kg}^{-1} \text{ K}^{-1}$ (vs $199 \text{ J kg}^{-1} \text{ K}^{-1}$ of cGST). Hence, with the same heater design, we would expect even faster switching speed of cSbS than cGST, though more energy is required for the amorphization, which can be achieved by using higher voltage pulses without increasing the pulse length.

Finally, we compare the performance metrics of our SbS integrated photonic switch to microring switches based on GST^[13] and GSST^[33] (Table 4). Although the SbS integrated switch uses an 8 μm -long SbS (vs 5 μm for GST), its insertion loss is estimated to be only 0.48 dB compared to 1.8 dB for GST (See Section S6, Supporting information for insertion loss estimation). The insertion loss of SbS-based microring switch is comparable to that based on GSST. However, PCM used in our devices is shorter and thinner which will help to reduce the total energy consumption required for phase transition. Note that ITO has non-negligible loss near 1550 nm. The GST here is capped with only 10 nm ITO while the SbS is capped

with 200 nm of ITO. If thinner ITO or a PIN^[44] heater is used instead, the insertion loss would expect to decrease further.

2.4. Thermo-Optic Effect of SbS

Due to the large positive thermo-optic (TO) effect of silicon,^[44] SOI platform is prone to thermal fluctuations, particularly for high- Q optical resonators.^[58] Integrated metal heaters near the resonators are normally used to stabilize the temperature and prevent resonance drift from the temperature variation in the environment.^[59,60] The TO effect of GST has already been investigated on SiN waveguides.^[61] Here, we showed that SbS exhibits strong negative TO effect that counteracts the positive TO effect of silicon. The overall TO coefficient of SbS–SOI hybrid waveguide is hence lower than pure Si waveguide, making the hybrid system more thermally stable. By heating the ring resonators capped with different lengths of SbS, the TO coefficient of SbS on SOI is extracted in both amorphous and crystalline states near 1550 nm. Thicker SbS (66nm) is used to amplify the minimal change in resonance spectrum from the TO effect of SbS. Note that the PCM is only placed on top of the waveguide to simplify the calculation of mode confinement factor (Figure 2c,d). The TO coefficient of SbS–SOI hybrid waveguide can be approximated to the first order as:^[62]

$$\frac{dn_{\text{eff}}}{dT} = \Gamma_{\text{Si}}(\lambda) \frac{dn_{\text{Si}}}{dT}(\lambda) + \Gamma_{\text{SbS}} \frac{dn_{\text{SbS}}}{dT}(\lambda) \quad (3)$$

where the mode confinement factors Γ ^[63] of Si waveguide and SbS are wavelength dependent and can be calculated using Lumerical mode solutions (see Section S7, Supporting information). By adjusting the temperature of a thermal electric controller beneath the chip, we can tune the resonances (Figure 5a). Using the resonance shift and the temperature change, the collective TO coefficient of SbS–Si hybrid waveguide can be expressed as (see Section S7, Supporting information for derivation):

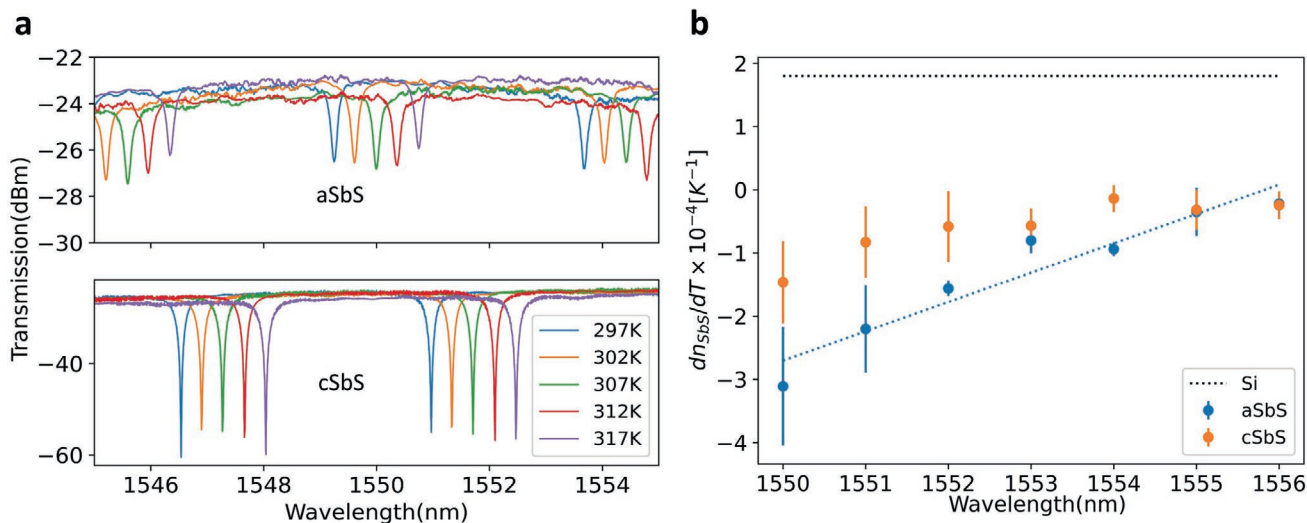


Figure 5. Thermo-optic effect of SbS on SOI. a) Spectral shift caused by raising the temperature from 297 to 317 K of microring capped with 10 μm -long, 66 nm-thick SbS. b) Extracted thermo-optic coefficient of aSbS and cSbS compared with silicon.

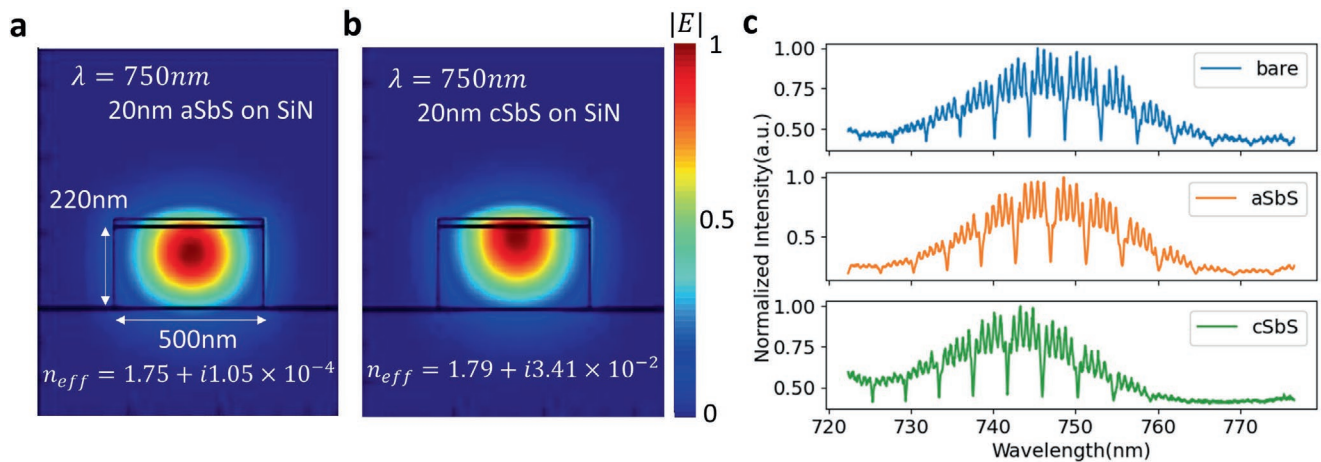


Figure 6. SbS on SiN microrings. a) Simulated fundamental quasi-TE mode profiles of 20 nm aSbS/cSbS on SiN hybrid waveguide at 750 nm. Note here that the SbS is only placed on top of the waveguide. b) Transmission spectrum of SiN ring resonators capped with 5 μm aSbS and cSbS near 750 nm.

$$\frac{dn_{eff}}{dT} = \left(\frac{\lambda_{res} n_{eff}^{Si}}{\lambda_{res0} \Delta T} - \frac{n_{eff}^{Si}}{dT} - \frac{dn_{eff}^{Si}}{dT} \right) \frac{2\pi R - L_{SbS}}{L_{SbS}} + \left(\frac{\lambda_{res}}{\lambda_{res0}} - 1 \right) \frac{n_{eff0}}{\Delta T} \quad (4)$$

Note that $\frac{dn_{eff}}{dT}$ and $\frac{dn_{eff}^{Si}}{dT}$ in Equation (4) not only describe the TO effect of SbS–SOI hybrid waveguide and Si waveguide, but also include the effect of dispersion which must be subtracted to extract the pure temperature effect to the refractive index. n_{eff0} and n_{eff}^{Si} are the effective indices of SbS–Si hybrid waveguide and SOI waveguide respectively at the resonance wavelength before the temperature change of ΔT . λ_{res0} and λ_{res} are the resonance wavelengths before and after the temperature change, respectively. Substituting Equation (3) into Equation (4) hence yields the expression of TO coefficient of pristine SbS in terms of the measurable parameters λ_{res0} , λ_{res} , and ΔT . Here, the length of the SbS is varied from 0 to 80 μm (nine rings) and each device is measured at five different temperatures (i.e., for four ΔT s) from 297 to 317 K, giving four values of TO coefficient for each length of SbS. No definite dependency of SbS TO coefficient on temperature is observed in the experiment. Hence, it is assumed that the change in the TO coefficient with temperature is negligible for both Si and SbS in this temperature range. Figure 5b shows the wavelength dependent TO coefficients of both amorphous and crystalline SbS compared with Si near 1550 nm.^[41] The data points are calculated as the average of TO coefficients across four ΔT s while the error bars measure the standard deviation from the average of four. The TO coefficient of aSbS exhibits a strong linear dependency to wavelength, whereas the TO coefficient of cSbS is wavelength independent. The TO coefficient of aSbS and cSbS at 1550 nm are estimated to be $-3.11 \times 10^{-4} \text{ K}^{-1}$ and $-7.28 \times 10^{-5} \text{ K}^{-1}$. The strong negative TO effect of SbS shows that the SbS–SOI hybrid platform has less sensitivity to heat fluctuation than SOI does and is suitable for use in non-volatile integrated photonics.

2.5. SbS on SiN Microring Resonators

Finally, since SbS is transparent near visible wavelengths, the tuning ability of SbS on SiN platform is also investigated.

Specifically, we probed the wavelength regime near 750 nm, where quantum emitters like SiV in diamond^[64] and quantum materials like WSe₂ emit.^[65] A second chip was fabricated (See Experimental Section) on SiN-on-oxide platform with similar design to probe the optical properties of SbS near 750 nm. The wide bandgap of SiN makes it transparent in the visible wavelengths and is widely used in integrated quantum optics.^[62,66] Figure 6a,b shows the mode simulation of 20 nm SbS on SiN at 750 nm wavelength where the effective index change $\Delta n_{eff} = 0.04$ is nearly two times that of SbS on SOI at 1550 nm. The theoretically calculated $\Delta\lambda$ is $0.273 \text{ nm } \mu\text{m}^{-1}$ and the loss is $2.48 \text{ dB } \mu\text{m}^{-1}$. Figure 6c shows the transmission spectrum of 5 μm-long SbS on SiN ring (10 μm radius) before and after thermal annealing. Owing to low optical losses, the resonances are clearly visible in both amorphous and crystalline states from 720 to 770 nm whereas the same length of GST will completely destroy the resonances. Hence, our experiment demonstrates the unlimited potential of SbS to be used in tunable visible integrated photonics. We note that the experimentally extracted $\Delta\lambda$ and loss of cSbS do not match quite well with the simulation (see Section S7, Supporting information) and further experiments are planned to characterize the exact optical phase modulation effect of SbS near 750 nm.

3. Conclusion

In this paper, an emerging wide-bandgap phase change material Sb₂S₃ is investigated for its applications in non-volatile reconfigurable photonics. The XRD and Raman data have confirmed the phase transition of Sb₂S₃ from amorphous to crystalline state while ellipsometry shows that the material exhibits broadband transparency from 610 nm to near-IR. The large refractive index contrast and low absorptive loss of Sb₂S₃ are verified experimentally for the first time on SOI and SiN integrated photonics platform using microring resonators at the telecom C-band and near visible wavelengths. The measured resonance shift is $0.06 \text{ nm } \mu\text{m}^{-1}$ at 1550 nm while the optical losses at 1550 nm are $0.16 \text{ dB } \mu\text{m}^{-1}$ in crystalline state and zero in amorphous state. An on-chip non-volatile Sb₂S₃–SOI

microring switch with low-loss, large optical phase shift ($\Delta\lambda \approx 0.4$ nm) and extinction ratio (>30dB) is demonstrated. Although the switching speed is slow for now (1s for SET and 200 ns for RESET), we believe the switching speed can approach tens of nanoseconds with more thermally stable heater material and optimized heater design. For example, the waveguides can be planarized to reduce the required heater material thickness or atomically thin heater such as graphene can be used. Once high cyclability is achieved, more work will be done to characterize the transient response of the photonic switch in the nanosecond range to investigate how the optical transmission varies with electrical excitation, similar to the analysis in our previous work.^[14] Additionally, the thermo-optic coefficient of aSbS and cSbS at 1550 nm is extracted to be $-3.11 \times 10^{-4} \text{ K}^{-1}$ and $-7.28 \times 10^{-5} \text{ K}^{-1}$, respectively, with opposite sign to that of Si, showing that the SbS–SOI hybrid waveguide is more stable to temperature variation than Si waveguide. Potential future work will aim to show the electrical tunability of Sb_2S_3 on integrated SiN platform near 750 nm as well as large endurance of Sb_2S_3 integrated photonic switches. Guided by the performance metrics map for optical PCMs,^[67] other emerging low-loss PCMs such as Sb_2Se_3 ^[34,43] may also be explored. Our experiments introduce Sb_2S_3 as a promising candidate for the low loss non-volatile tuning of large-scale PIC at lower energy consumption and smaller footprint and will find wide applications in fields such as optical FPGAs, post-fabrication trimming, and non-volatile quantum integrated optics.

4. Experimental Section

SOI Device Fabrication: The SbS-on-SOI microring resonators were fabricated on a 220-nm thick silicon layer on top of a 3- μm -thick buried oxide layer (SOITECH). The pattern was defined by a JEOLJBX-6300FS 100 kV electron-beam lithography (EBL) system using positive tone ZEP-520A resist. 220 nm fully etched ridge waveguides were made by an inductively coupled plasma reactive ion etching (ICP-RIE) process. A second EBL exposure using positive tone poly(methyl methacrylate) (PMMA) resist was subsequently carried out to create windows for the SbS deposition. After development, 20 nm SbS was DC sputtered from a SbS target (Plasmaterial Ltd.) in a magnetron Sputter System (Lesker Lab18) under Ar atmosphere at 27 W and base pressure of $\approx 5 \times 10^{-7}$ Torr. The Ar flow rate was controlled to maintain a sputtering pressure of 3.5 mTorr. The plasma was stabilized for 5 min before the actual deposition. The lift-off of SbS was completed using methylene chloride followed by a global capping of 10 nm PECVD SiN at 125 °C to prevent oxidation. Note that the SbS samples used for ellipsometry, Raman, and XRD were deposited on Si [100] wafers and capped with 10 nm sputtered ITO. The SbS–ITO integrated photonic switch was fabricated in a similar process where the waveguide was only partially etched by 140 nm for easier liftoff of ITO. A 200 nm thick ITO layer was sputtered following the 20 nm SbS deposition without breaking vacuum. After the lift-off of the SbS/ITO layers, an extra EBL overlay and electron beam evaporation of Au/Cr (60 nm/30 nm) were done to pattern the electrode pads. For crystallization of SbS, rapid thermal annealing (RTA) at 300 °C for 20 min was performed under N₂ atmosphere.

SiN Device Fabrication: The SiN microring resonators were fabricated on a 220-nm-thick SiN membrane grown via LPCVD on 4 μm of thermal oxide on silicon (Rogue Valley Microelectronics). Roughly 400 nm of ZEP520A was spun, which was coated with a thin layer of Pt/Au that served as a charging layer. The resist was then patterned by EBL and the pattern was transferred to the SiN using the same RIE in CHF_3/O_2 chemistry. The SbS was deposited onto the SiN rings using the same process mentioned above.

Experimental Setup: The microrings on SOI were characterized by a vertical fiber-coupling setup.^[14] All the measurements were performed under ambient conditions while the temperature of the stage was fixed at ≈ 24 °C by a thermoelectric controller (TEC, TE Technology TC-720) to prohibit the serious thermal shift of the resonators. The input light was provided by a tunable continuous-wave laser (Santec TSL-510) and its polarization was controlled by a manual fiber polarization controller (Thorlabs FPC526) to match the fundamental quasi-TE mode of the waveguides.

A low-noise power meter (Keysight 81634B) was used to collect the static optical output from the grating couplers. The transmission spectrum measurement was performed after the fabrication of bare ring resonators, deposition of SbS, and annealing, respectively to extract the spectral shift and change in optical loss in each step. For the electrical characterization of SbS–ITO photonic switch, the electrical signals were applied to the metal contacts by a pair of DC probes controlled by two probe positioners (Cascade Microtech DPP105-M-AI-S). The current sweep and voltage measurement were provided by a source meter (Keithley 2450) and the Reset pulses were generated from a pulse function arbitrary generator (Keysight 81160A).

The SiN microrings were characterized via measuring the transmission using a confocal microscopy setup.^[62] A super continuum light source (Fianium WhiteLase Micro) was focused on the grating coupler through the objective lens, and a moveable pinhole was used to pick up only the signal coming out from the other grating and then send it to a spectrometer. The spectrometer was equipped with a Princeton Instruments PIXIS CCD with an IsoPlane SCT-320 Imaging Spectrograph.

Supporting Information

Supporting Information is available from the Wiley Online Library or from the author.

Acknowledgements

Z.F. and A.M. conceived the project. Z.F. simulated, designed, and fabricated the devices. Z. F. performed the experiments. J.Z. helped with the experiments and simulations. A.S. performed the SiN optical measurements. J.W. helped with the SEM imaging. Y.C. advised on the SiN fabrication. A.M. supervised the overall progress of the project. Z.F. wrote the manuscript with input from all the authors. The research is funded by National Science Foundation (NSF-1640986, NSF-2003509), and ONR-YIP Award. Part of this work was conducted at the Washington Nanofabrication Facility/ Molecular Analysis Facility, a National Nanotechnology Coordinated Infrastructure (NNCI) site at the University of Washington, which is supported in part by funds from the National Science Foundation (awards NNCI-1542101, 1337840 and 0335765), the National Institutes of Health, the Molecular Engineering & Sciences Institute, the Clean Energy Institute, the Washington Research Foundation, the M. J. Murdock Charitable Trust, Altatech, ClassOne Technology, GCE Market, Google, and SPTS.

Conflict of Interest

The authors declare no conflict of interest.

Data Availability Statement

The data that support the findings of this study are available from the corresponding author upon reasonable request.

Keywords

integrated photonics, phase change materials, reconfigurable optics, silicon photonics

Received: November 30, 2020

Revised: February 8, 2021

Published online:

- [1] M. R. Watts, J. Sun, C. DeRose, D. C. Trotter, R. W. Young, G. N. Nielson, *Opt. Lett.* **2013**, *38*, 733.
- [2] W. M. J. Green, M. J. Rooks, L. Sekaric, Y. A. Vlasov, *Opt. Express* **2007**, *15*, 17106.
- [3] D. J. Thomson, F. Y. Gardes, J. Fedeli, S. Zlatanovic, Y. Hu, B. P. P. Kuo, E. Myslivets, N. Alic, S. Radic, G. Z. Mashanovich, G. T. Reed, *IEEE Photonics Technol. Lett.* **2012**, *24*, 234.
- [4] W. Bogaerts, D. Pérez, J. Capmany, D. A. B. Miller, J. Poon, D. Englund, F. Morichetti, A. Melloni, *Nature* **2020**, *586*, 207.
- [5] L. Alloatti, R. Palmer, S. Diebold, K. P. Pahl, B. Chen, R. Dinu, M. Fournier, J.-M. Fedeli, T. Zwick, W. Freude, C. Koos, J. Leuthold, *Light: Sci. Appl.* **2014**, *3*, e173.
- [6] C. Koos, P. Vorreau, T. Vallaitis, P. Dumon, W. Bogaerts, R. Baets, B. Esembeson, I. Biaggio, T. Michinobu, F. Diederich, W. Freude, J. Leuthold, *Nat. Photonics* **2009**, *3*, 216.
- [7] S. Koeber, R. Palmer, M. Laueremann, W. Heni, D. L. Elder, D. Korn, M. Woessner, L. Alloatti, S. Koenig, P. C. Schindler, H. Yu, W. Bogaerts, L. R. Dalton, W. Freude, J. Leuthold, C. Koos, *Light: Sci. Appl.* **2015**, *4*, e255.
- [8] C. Wang, M. Zhang, X. Chen, M. Bertrand, A. Shams-Ansari, S. Chandrasekhar, P. Winzer, M. Lončar, *Nature* **2018**, *562*, 101.
- [9] M. He, M. Xu, Y. Ren, J. Jian, Z. Ruan, Y. Xu, S. Gao, S. Sun, X. Wen, L. Zhou, L. Liu, C. Guo, H. Chen, S. Yu, L. Liu, X. Cai, *Nat. Photonics* **2019**, *13*, 359.
- [10] C. Haffner, A. Joerg, M. Doderer, F. Mayor, D. Chelladurai, Y. Fedoryshyn, C. I. Roman, M. Mazur, M. Burla, H. J. Lezec, V. A. Aksyuk, J. Leuthold, *Science* **2019**, *366*, 860.
- [11] R. Amin, R. Maiti, Y. Gui, C. Suer, M. Miscuglio, E. Heidari, R. T. Chen, H. Dalir, V. J. Sorger, *Optica* **2020**, *7*, 333.
- [12] A. Emboras, I. Goykhman, B. Desiatov, N. Mazurski, L. Stern, J. Shappir, U. Levy, *Nano Lett.* **2013**, *13*, 6151.
- [13] J. Zheng, A. Khanolkar, P. Xu, S. Colburn, S. Deshmukh, J. Myers, J. Frantz, E. Pop, J. Hendrickson, J. Doyle, N. Boechler, A. Majumdar, *Opt. Mater. Express* **2018**, *8*, 1551.
- [14] J. Zheng, Z. Fang, C. Wu, S. Zhu, P. Xu, J. K. Doyle, S. Deshmukh, E. Pop, S. Dunham, M. Li, A. Majumdar, *Adv. Mater.* **2020**, *32*, 2001218.
- [15] C. Ríos, M. Stegmaier, P. Hosseini, D. Wang, T. Scherer, C. D. Wright, H. Bhaskaran, W. H. P. Pernice, *Nat. Photonics* **2015**, *9*, 725.
- [16] J. Feldmann, M. Stegmaier, N. Gruhler, C. Ríos, H. Bhaskaran, C. D. Wright, W. H. P. Pernice, *Nat. Commun.* **2017**, *8*, 1256.
- [17] J. Feldmann, N. Youngblood, C. D. Wright, H. Bhaskaran, W. H. P. Pernice, *Nature* **2019**, *569*, 208.
- [18] K. Shportko, S. Kremers, M. Woda, D. Lencer, J. Robertson, M. Wuttig, *Nat. Mater.* **2008**, *7*, 653.
- [19] M. Wuttig, N. Yamada, *Nat. Mater.* **2007**, *6*, 824.
- [20] S. Raoux, F. Xiong, M. Wuttig, E. Pop, *MRS Bull.* **2014**, *39*, 703.
- [21] D. Loke, T. H. Lee, W. J. Wang, L. P. Shi, R. Zhao, Y. C. Yeo, T. C. Chong, S. R. Elliott, *Science* **2012**, *336*, 1566.
- [22] F. Xiong, A. D. Liao, D. Estrada, E. Pop, *Science* **2011**, *332*, 568.
- [23] S. Abdollahramezani, O. Hemmatyar, H. Taghinejad, A. Krasnok, Y. Kiarashinejad, M. Zandehshavar, A. Alù, A. Adibi, *Nanophotonics* **2020**, <https://doi.org/10.1515/nanoph-2020-0039>.
- [24] Y. Shen, N. C. Harris, S. Skirlo, M. Prabhu, T. Baehr-Jones, M. Hochberg, X. Sun, S. Zhao, H. Larochelle, D. Englund, M. Soljačić, *Nat. Photonics* **2017**, *11*, 441.
- [25] J. Wang, S. Paesani, Y. Ding, R. Santagati, P. Skrzypczyk, A. Salavrakos, J. Tura, R. Augusiak, L. Mančinska, D. Bacco, D. Bonneau, J. W. Silverstone, Q. Gong, A. Acín, K. Rottwitz, L. K. Oxenløwe, J. L. O'Brien, A. Laing, M. G. Thompson, *Science* **2018**, *360*, 285.
- [26] D. Pérez, I. Gasulla, L. Crudgington, D. J. Thomson, A. Z. Khokhar, K. Li, W. Cao, G. Z. Mashanovich, J. Capmany, *Nat. Commun.* **2017**, *8*, 636.
- [27] W. Zhang, J. Yao, *Nat. Commun.* **2020**, *11*, 406.
- [28] P. Xu, J. Zheng, J. K. Doyle, A. Majumdar, *ACS Photonics* **2019**, *6*, 553.
- [29] Q. Zhang, Y. Zhang, J. Li, R. Soref, T. Gu, J. Hu, *Opt. Lett.* **2018**, *43*, 94.
- [30] W. Dong, H. Liu, J. K. Behera, L. Lu, R. J. H. Ng, K. V. Sreekanth, X. Zhou, J. K. W. Yang, R. E. Simpson, *Adv. Funct. Mater.* **2019**, *29*, 1806181.
- [31] A. H. Atabaki, A. A. Eftekhar, M. Askari, A. Adibi, *Opt. Express* **2013**, *21*, 14139.
- [32] J.-H. Kim, S. Aghaeimeibodi, J. Carolan, D. Englund, E. Waks, *Optica* **2020**, *7*, 291.
- [33] Y. Zhang, J. B. Chou, J. Li, H. Li, Q. Du, A. Yadav, S. Zhou, M. Y. Shalaginov, Z. Fang, H. Zhong, C. Roberts, P. Robinson, B. Bohlin, C. Ríos, H. Lin, M. Kang, T. Gu, J. Warner, V. Liberman, K. Richardson, J. Hu, *Nat. Commun.* **2019**, *10*, 4279.
- [34] M. Delaney, I. Zeimpekis, D. Lawson, D. W. Hewak, O. L. Muskens, *Adv. Funct. Mater.* **2020**, *30*, 2002447.
- [35] P. Arun, A. G. Vedeshwar, *J. Appl. Phys.* **1996**, *79*, 4029.
- [36] X. Shuai, W. Shen, *Nanoscale Res. Lett.* **2012**, *7*, 199.
- [37] B. Krishnan, A. Arato, E. Cardenas, T. K. D. Roy, G. A. Castillo, *Appl. Surf. Sci.* **2008**, *254*, 3200.
- [38] R. Parize, T. Cossuet, O. Chaix-Pluchery, H. Roussel, E. Appert, V. Consonni, *Mater. Des.* **2017**, *121*, 1.
- [39] Z. Fang, University of Oxford, Investigation into the Properties and Electrical Switching Performance of Ge₂Sb₂Se₄Te₁, **2017**.
- [40] Z. Fang, T. Gu, J. Hu, J. Li, Y. Zhang, US20180284492A1, **2018**.
- [41] J. Komma, C. Schwarz, G. Hofmann, D. Heinert, R. Nawrodt, *Appl. Phys. Lett.* **2012**, *101*, 041905.
- [42] J. Zheng, S. Zhu, P. Xu, S. Dunham, A. Majumdar, *ACS Appl. Mater. Interfaces* **2020**, *12*, 21827.
- [43] M. Delaney, I. Zeimpekis, H. Du, X. Yan, M. Banakar, D. J. Thomson, D. W. Hewak, O. L. Muskens, arXiv:2101.03623 [physics.optics], **2021**.
- [44] M. Stegmaier, C. Ríos, H. Bhaskaran, C. D. Wright, W. H. P. Pernice, *Adv. Opt. Mater.* **2017**, *5*, 1600346.
- [45] H. Zhang, L. Zhou, L. Lu, J. Xu, N. Wang, H. Hu, B. M. A. Rahman, Z. Zhou, J. Chen, *ACS Photonics* **2019**, *6*, 2205.
- [46] N. Farmakidis, N. Youngblood, X. Li, J. Tan, J. L. Swett, Z. Cheng, C. D. Wright, W. H. P. Pernice, H. Bhaskaran, *Sci. Adv.* **2019**, *5*, eaaw2687.
- [47] P. Hosseini, C. D. Wright, H. Bhaskaran, *Nature* **2014**, *511*, 206.
- [48] H. Taghinejad, S. Abdollahramezani, A. A. Eftekhar, T. Fan, A. H. Hosseini, O. Hemmatyar, A. E. Dorche, A. Gallmon, A. Adibi, arXiv:2003.04097 [physics.app-ph], **2020**.
- [49] K. Kato, M. Kuwahara, H. Kawashima, T. Tsuruoka, H. Tsuda, *Appl. Phys. Express* **2017**, *10*, 072201.
- [50] Q. Xu, B. Schmidt, S. Pradhan, M. Lipson, *Nature* **2005**, *435*, 325.
- [51] J. Kim, S. Shrestha, M. Souri, J. G. Connell, S. Park, A. Seo, *Sci. Rep.* **2020**, *10*, 12486.
- [52] T. Kawashima, T. Ezure, K. Okada, H. Matsui, K. Goto, N. Tanabe, *J. Photochem. Photobiol., A* **2004**, *164*, 199.
- [53] H. Liu, W. Dong, H. Wang, L. Lu, Q. Ruan, Y. S. Tan, R. E. Simpson, J. K. W. Yang, *Sci. Adv.* **2020**, *6*, eabb7171.

- [54] C. Ríos, Y. Zhang, M. Y. Shalaginov, S. Deckoff-Jones, H. Wang, S. An, H. Zhang, M. Kang, K. A. Richardson, C. Roberts, J. B. Chou, V. Liberman, S. A. Vitale, J. Kong, T. Gu, J. Hu, *Adv. Photonics Res.* **2021**, 2, 2000034.
- [55] N. Youngblood, C. Talagrand, B. Porter, C. G. Galante, S. Kneepkens, S. G. Sarwat, D. Yarmolich, R. S. Bonilla, P. Hosseini, R. Taylor, H. Bhaskaran, arXiv:1911.02990 [physics.app-ph], **2019**.
- [56] Y. Kawamoto, H. Iwasaki, *J. Electron. Mater.* **2014**, 43, 1475.
- [57] G. K. Johnson, G. N. Papatheodorou, C. E. Johnson, *J. Chem. Thermodyn.* **1981**, 13, 745.
- [58] J. Zhou, J. Zheng, Z. Fang, P. Xu, A. Majumdar, *Opt. Express* **2019**, 27, 30692.
- [59] C. Sun, M. T. Wade, Y. Lee, J. S. Orcutt, L. Alloatti, M. S. Georgas, A. S. Waterman, J. M. Shainline, R. R. Avizienis, S. Lin, B. R. Moss, R. Kumar, F. Pavanello, A. H. Atabaki, H. M. Cook, A. J. Ou, J. C. Leu, Y.-H. Chen, K. Asanović, R. J. Ram, M. A. Popović, V. M. Stojanović, *Nature* **2015**, 528, 534.
- [60] A. H. Atabaki, S. Moazeni, F. Pavanello, H. Gevorgyan, J. Notaros, L. Alloatti, M. T. Wade, C. Sun, S. A. Kruger, H. Meng, K. Al Qubaisi, I. Wang, B. Zhang, A. Khilo, C. V. Baiocco, M. A. Popović, V. M. Stojanović, R. J. Ram, *Nature* **2018**, 556, 349.
- [61] M. Stegmaier, C. Ríos, H. Bhaskaran, W. H. P. Pernice, *ACS Photonics* **2016**, 3, 828.
- [62] Y. Chen, J. Whitehead, A. Ryou, J. Zheng, P. Xu, T. Fryett, A. Majumdar, *Opt. Lett.* **2019**, 44, 3058.
- [63] J. T. Robinson, K. Preston, O. Painter, M. Lipson, *Opt. Express* **2008**, 16, 16659.
- [64] C. Bradac, W. Gao, J. Forneris, M. E. Trusheim, I. Aharonovich, *Nat. Commun.* **2019**, 10, 5625.
- [65] S. Wu, S. Buckley, J. R. Schaibley, L. Feng, J. Yan, D. G. Mandrus, F. Hatami, W. Yao, J. Vučković, A. Majumdar, X. Xu, *Nature* **2015**, 520, 69.
- [66] Y. Chen, A. Ryou, M. R. Friedfeld, T. Fryett, J. Whitehead, B. M. Cossairt, A. Majumdar, *Nano Lett.* **2018**, 18, 6404.
- [67] B. J. Kooi, M. Wuttig, *Adv. Mater.* **2020**, 32, 1908302.